

# Seasonal Superrotation in Earth's Troposphere

Pengcheng Zhang<sup>1,1</sup> and Nicholas J Lutsko<sup>1,1</sup>

<sup>1</sup>University of California San Diego

November 30, 2022

## Abstract

Although Earth's troposphere does not superrotate in the annual-mean, for most of the year – from October to May – the winds of the tropical upper troposphere are westerly. We investigate this seasonal superrotation using reanalysis data and a single-layer model for the winds of the tropical upper troposphere. The temporal and spatial structures of the tropospheric superrotation are characterized, and the relationships between the superrotation and the leading modes of tropical interannual variability are quantified. It is also shown that the strength of the superrotation has remained roughly constant over the past few decades, despite the winds of the tropical upper troposphere decelerating (becoming more easterly) in other months. The underlying dynamics of the seasonal superrotation are studied using a combination of momentum budget analysis and numerical simulations with an axisymmetric, single-layer model of the tropical upper troposphere. Momentum flux convergence by stationary eddies accelerates the superrotation, while cross-equatorial easterly momentum transport associated with the Hadley circulation decelerates the superrotation. The seasonal modulations of these two competing factors shape the superrotation. The single-layer model is able to qualitatively reproduce the seasonal progression of the winds in the tropical upper troposphere, and highlights the northward displacement of the Intertropical Convergence Zone in the annual-mean as a key factor responsible for the annual cycle of the tropical winds.

# Seasonal Superrotation in Earth's Troposphere

Pengcheng Zhang<sup>a</sup>, Nicholas J. Lutsko<sup>a</sup>

<sup>a</sup> *Scripps Institution of Oceanography, University of California San Diego, La Jolla, CA, USA*

<sup>4</sup> *Corresponding author:* Pengcheng Zhang, pczhang@ucsd.edu

5 ABSTRACT: Although Earth’s troposphere does not superrotate in the annual-mean, for most  
6 of the year – from October to May – the winds of the tropical upper troposphere are westerly.  
7 We investigate this seasonal superrotation using reanalysis data and a single-layer model for the  
8 winds of the tropical upper troposphere. The temporal and spatial structures of the tropospheric  
9 superrotation are characterized, and the relationships between the superrotation and the leading  
10 modes of tropical interannual variability are quantified. It is also shown that the strength of the  
11 superrotation has remained roughly constant over the past few decades, despite the winds of the  
12 tropical upper troposphere decelerating (becoming more easterly) in other months. The underlying  
13 dynamics of the seasonal superrotation are studied using a combination of momentum budget  
14 analysis and numerical simulations with an axisymmetric, single-layer model of the tropical upper  
15 troposphere. Momentum flux convergence by stationary eddies accelerates the superrotation, while  
16 cross-equatorial easterly momentum transport associated with the Hadley circulation decelerates  
17 the superrotation. The seasonal modulations of these two competing factors shape the superrotation.  
18 The single-layer model is able to qualitatively reproduce the seasonal progression of the winds  
19 in the tropical upper troposphere, and highlights the northward displacement of the Intertropical  
20 Convergence Zone in the annual-mean as a key factor responsible for the annual cycle of the tropical  
21 winds.

## 1. Introduction

Superrotation refers to a state in which an atmosphere has greater angular momentum than its planet’s surface at the equator. That is, superrotation requires that the zonal-mean zonal wind  $U$  satisfies  $U > U_m$ , where

$$U_m = \Omega a \sin^2(\phi) / \cos \phi, \quad (1)$$

with  $\Omega$  as the planet’s rotation rate,  $a$  as the planet’s radius and  $\phi$  as latitude. Superrotation usually manifests as westerly zonal-mean winds over the equator, as off-equatorial angular momentum maxima are inertially unstable (e.g., see Eliassen and Kleinschmidt 1957).

Atmospheric superrotation is seen in a wide variety of planetary contexts. The atmospheres of Venus (Belton et al. 1991; Peralta et al. 2007; Horinouchi et al. 2020) and Titan (Bird et al. 2005; Kostiuk et al. 2006) are observed to superrotate, while two of the gas giants in the solar system, Jupiter and Saturn, have superrotating atmospheres relative to the rotation of their magnetic fields (Seiff 2000; Genio et al. 2009; note that the concept of superrotation on gas giants is ambiguous because gas giants don’t have a well-defined surface). Outside the Solar System, the atmospheres of many tidally-locked gas giants and terrestrial exoplanets are expected to superrotate (Showman and Polvani 2011; Tsai et al. 2014; Pierrehumbert and Hammond 2019), and on Earth superrotation has been linked to the possible “permanent El Niño-like” state of the tropical Pacific during the Pliocene (Tziperman and Farrell 2009) and also appears in simulations of extreme global warming scenarios (Caballero and Huber 2010; Laraia and Schneider 2015).

Hide’s theorem says that superrotation must be maintained by upgradient angular momentum fluxes (Hide 1969, 1970; Gierasch 1975; Held and Hou 1980; Schneider 2006), which suggests that eddies must be involved for an atmosphere to achieve superrotation. One possible mechanism of eddy generation is stationary or propagating vorticity sources in the deep tropics. A number of studies have investigated superrotation associated with localized tropical heating, motivated in some cases by the dynamics of tidally-locked exoplanets (Suarez and Duffy 1992; Saravanan 1993; Hoskins et al. 1999; Kraucunas and Hartmann 2005; Norton 2006; Adames and Wallace 2017; Caballero and Huber 2010; Showman and Polvani 2010; Arnold et al. 2011; Lutsko 2017; Herbert et al. 2020). The wave response to tropical heating is generally found to be similar to the classic Matsuno-Gill model (Matsuno 1966; Gill 1980), though Showman and Polvani (2010)

50 demonstrated that vertical momentum exchange must be added to the Matsuno-Gill model in order  
51 for there to be net momentum convergence onto the equator. Showman and Polvani (2011) and  
52 Pinto and Mitchell (2016) further argued that equatorial waves are mostly trapped in the tropics,  
53 and so focused on the role of phase tilts due to differential zonal propagation of equatorial waves,  
54 rather than meridional propagation, for generating equatorward momentum fluxes.

55 Alternatively, eddies can be generated spontaneously in the deep tropics due to instabilities,  
56 without explicit tropical forcing. This has been seen in simulations of small and/or slowly rotating  
57 planets with axisymmetric thermal forcing, for which transient eddies converge momentum onto  
58 the equator and drive superrotation (see Wang and Mitchell 2014 and Lewis et al. 2021 for  
59 the dependence of superrotation on planetary rotation rate). Our understanding of the nature  
60 of the instabilities driving these transient eddies has evolved. Spontaneous superrotation was  
61 first attributed to classic barotropic instability (e.g., Williams 2003; Mitchell and Vallis 2010),  
62 whereas more recent literature (e.g., Potter et al. 2013; Wang and Mitchell 2014; Zurita-Gotor  
63 and Held 2018; Zurita-Gotor et al. 2022) has suggested the equatorial acceleration is due to an  
64 ageostrophic Rossby-Kelvin instability (see Sakai 1989 for a detailed description of the Rossby-  
65 Kelvin instability). Equatorial superrotation can be further enhanced by a reduction in the breaking  
66 of baroclinic eddies originating in mid-latitudes, which decelerates the flow in the tropics under  
67 Earth-like conditions (Laraia and Schneider 2015; Polichtchouk and Cho 2016).

68 On Earth, the stratosphere superrotates during the westerly phase of the Quasi-Biennial Os-  
69 cillation (QBO, see Baldwin et al. 2001), but the climatological winds of the troposphere do not  
70 superrotate. The reason for the lack of annual-mean superrotation was first identified by Lee (1999),  
71 who showed that the seasonal cycle of the Hadley circulation is crucial for decelerating the flow,  
72 as the cross-equatorial flow brings air with low angular momentum across the equator, especially  
73 during the solstitial seasons (see also Dima et al. 2005; Yang et al. 2013). Alternatively, we note  
74 that the annual-mean Intertropical Convergence Zone (ITCZ) is located north of the equator and  
75 so, assuming that the strongest zonal-mean ascent occurs in the ITCZ, the dynamics of an angular  
76 momentum-conserving Hadley circulation require that the annual-mean zonal flow in the equato-  
77 rial upper troposphere be easterly (see e.g., Held and Hou 1980; Lindzen and Hou 1988; Hill et al.  
78 2019). Although the observed Hadley circulation is not strictly angular momentum-conserving,

79 the hemispheric differences which cause the ITCZ to be located off the equator in the annual-mean  
80 can also be said to prevent Earth’s troposphere from superrotating.

81 Nevertheless, while Earth’s tropical troposphere does not superrotate in the annual-mean, it does  
82 superrotate on seasonal time-scales. For example, Figure 1 of Zurita-Gotor (2019) shows that the  
83 vertically-integrated equatorial winds between 300-150 hPa superrotate from November to March<sup>1</sup>.  
84 By Hide’s theorem, this means that eddies must be converging momentum onto the equator, and that  
85 this momentum convergence overcomes the deceleration by the mean flow, even during the winter  
86 solstice. Zurita-Gotor (2019) studied the mechanisms of meridional eddy momentum transport  
87 in the tropics in detail, but did not characterize the spatial and temporal structure of the seasonal  
88 tropospheric superrotation or investigate how the eddy momentum flux interacts with the other  
89 terms in the momentum budget.

90 The present study investigates the seasonal superrotation of Earth’s tropical upper troposphere  
91 using a combination of reanalysis data and simple numerical simulations. The superrotation’s  
92 structure in time and space is characterized, and its potential relationships with leading modes of  
93 tropical variability are examined: superrotation is favored in La Niña years and during the easterly  
94 phase of the QBO. We identify stationary eddy momentum flux convergence as playing a crucial  
95 role in driving the superrotation, and are able to explain the seasonality of the superrotation using a  
96 simple numerical model. The eddy momentum flux convergence makes the superrotation possible  
97 during most of the year, while the strong cross-equatorial Hadley circulation prevents superrotation  
98 in boreal summer, producing the annual cycle of the upper tropospheric winds seen today. It is the  
99 dynamic balance between these two factors that shapes the characteristics and the seasonality of  
100 the superrotation.

101 The remainder of this paper is structured as follows. Section 2 introduces the datasets and nu-  
102 merical model we use. Section 3 describes the main characteristics of the seasonal superrotation in  
103 Earth’s tropical troposphere, including its structure, relationship with the major modes of interan-  
104 nual tropical variability, and recent trends. Section 4 analyzes the monthly-mean zonal momentum  
105 budgets to identify the drivers of the superrotation and to explain why it is only present for part  
106 of the year. In Section 5 we use a numerical model of the tropical upper troposphere to explore

---

<sup>1</sup>Interestingly, Dima et al. (2005) saw weak superrotation in October-November and April-May, but not in boreal winter. However, they used the older NCEP reanalysis, and below we confirm the superrotation in boreal winter using more recent reanalysis products.

how various factors contribute to the seasonal superrotation and to confirm our interpretation of the momentum budget analysis. We end in Section 6 with a summary and conclusions.

## 2. Methods

### *a. Data*

Daily wind speed data are obtained by averaging 3-hourly assimilated meteorological fields product (GMAO 2015) from the Modern-Era Retrospective Analysis for Research and Applications, Version 2 (MERRA-2, Gelaro et al. 2017). The data used in this study span the period 1980-2020 and pressure levels between 1000 hPa and 10 hPa. The MERRA-2 reanalysis uses a horizontal resolution of  $0.625^\circ \times 0.5^\circ$ , while the vertical grid spacing is 50 hPa in the mid- and upper-troposphere, which is the primary focus of this study.

To verify the robustness of the superrotation, we have repeated the analysis with three other reanalysis products: the European Centre for Medium-Range Weather Forecasts (ECMWF) Reanalysis v5 (ERA5,  $0.25^\circ \times 0.25^\circ$  resolution; Hersbach et al. 2020), the Japanese 55-year Reanalysis (JRA-55,  $1.25^\circ \times 1.25^\circ$  resolution; KOBAYASHI et al. 2015), and the National Center for Environmental Prediction Reanalysis 1 (NCEP-1,  $2.5^\circ \times 2.5^\circ$  resolution; Kalnay et al. 1996). The time span is 1980-2020 for all three reanalysis products, and the results are shown in the appendix.

To explore the relationship between the equatorial winds and the El-Niño Southern Oscillation (ENSO), we use the Oceanic Niño Index (ONI, see NOAA 2021) published by the National Oceanic and Atmospheric Administration's (NOAA<sup>2</sup>) Climate Prediction Center (CPC<sup>3</sup>). The ONI is based on the 3-month running mean of sea surface temperature (SST) anomalies in the Niño3.4 region ( $5^\circ\text{N}$ - $5^\circ\text{S}$ ,  $120^\circ\text{W}$ - $170^\circ\text{W}$ , see NOAA 2020). NOAA considers El Niño conditions to be present when the ONI is  $+0.5$  or higher, indicating the east-central tropical Pacific is significantly warmer than usual, and La Niña conditions to be present when the Oceanic Niño Index is  $-0.5$  or lower, indicating the region is cooler than usual (Dahlman 2016; NOAA 2021).

### *b. Single-layer model*

We use an axisymmetric single-layer model adapted from Sobel and Schneider (2009) (see also Sobel and Schneider 2013) to reconstruct and understand the superrotation. This model

---

<sup>2</sup><https://www.noaa.gov/>

<sup>3</sup><https://www.cpc.ncep.noaa.gov/>

was originally used to study interactions of the Hadley circulation with eddies, and is able to reproduce key qualitative features of the Hadley circulation in idealized GCM simulations. The model equations are

$$\partial_t u - v(\beta y - \partial_y u) = \mathcal{H}(\partial_y v)(\partial_y v)u - \mathcal{F} - \mathcal{S}, \quad (2)$$

$$2\partial_t v + \beta y u = -\frac{gH}{T_0} \partial_y T, \quad (3)$$

$$\partial_t \theta + \frac{\delta \Delta_z}{H} \partial_y v = \frac{\theta_E - \theta}{\tau}. \quad (4)$$

$u$  and  $v$  represent the zonal-mean zonal and meridional flow, respectively, in a thin layer below the tropopause of constant thickness  $\delta$  at constant height  $H$ . Potential temperature  $\theta$  and temperature  $T$  are related by  $\theta = T(p_s/p_t)^{R/c_p}$  with fixed tropopause and surface pressures  $p_t$  and  $p_s$  such that the constant factor  $(p_s/p_t)^{R/c_p} = 1.6$ . Also set fixed are the potential temperature difference  $\Delta_z$  between the surface and tropopause; the surface temperature  $T_0$ ; and the thermal relaxation time  $\tau$ . The radiative equilibrium (RE) temperature  $\theta_E = \theta_E(y, t)$  is a prescribed function of latitude and time;  $\mathcal{S}$  represents eddy momentum flux divergence (EMFD); and  $\mathcal{F} = \epsilon_u u$  represents frictional drag. The first term on the RHS of Eq. 2 corresponds to vertical momentum advection, where  $\mathcal{H}$  is the Heaviside function. Note that under the  $\beta$ -plane approximation, the  $y$  in this model is the distance from the equator in units of m.

In order to generate a realistic seasonal cycle, we prescribe a thermal forcing which varies in time as:

$$\theta_E = \begin{cases} \theta_{00} - \Delta_y \left[ \frac{y - y_0(t) - y_{am}}{y_1} \right]^2 & \text{if } |y| < y_1, \\ \theta_{00} - \Delta_y & \text{if } |y| \geq y_1, \end{cases} \quad (5)$$

where  $y_1 = 9439$  km ( $\sim 85$  degrees of latitude) and  $y_0(t)$  is the subsolar latitude over the course of the annual cycle, which takes the form

$$y_0(t) = y_M \sin \left[ \frac{2\pi}{t_a} (t - t_0) \right], \quad (6)$$

where  $t_a = 365$  is the length of a year in days,  $t_0 = 79$  is the spring equinox, and  $y_M$  is the subsolar latitude at the summer solstice, which we set to 2608 km ( $\sim 23.5^\circ\text{N}$ ).  $y_{am} = 666$  km ( $\sim 6^\circ\text{N}$ )

Parameter	Value	Definition
$\tau$	37 d	Thermal relaxation time
$H$	16 km	Tropopause height
$\delta$	4 km	Depth of layer
$T_0$	300 K	Reference surface temperature
$\Delta_z$	60 K	Vertical potential temperature stratification
$\Delta_y$	50 K	RE equator-pole temperature gradient
$\theta_{00}$	330 K	Background tropospheric-mean potential temperature
$\epsilon_u$	$10^{-8} \text{ s}^{-1}$	Background Rayleigh drag
$k_v$	$7.79 \times 10^4 \text{ m}^2/\text{s}$	Diffusivity
$\beta$	$2 \times 10^{-11} \text{ m}^{-1} \text{ s}^{-1}$	Meridional gradient of Coriolis parameter
$y_{am}$	666 km	Latitude of the annual-mean ITCZ
$y_0(t)$	Varying	Sub-solar latitudes
$t_0$	79	Spring equinox day in the year
$y_M$	2608 km	Sub-solar latitude at equinoxes

TABLE 1. Model parameter values used in this study.

denotes the latitude of the annual-mean Intertropical Convergence Zone (ITCZ) in today’s climate.

A complete list of parameter values is given in Table 1.

As in Sobel and Schneider 2009, the model is integrated on a staggered grid using a leapfrog time-stepping scheme. The domain contains 801 grid points for  $v$  and 800 grid points for  $u$  and  $\theta$ , for a resolution of 39.3 km. A second-order diffusion term, though not explicitly shown in the equations, is also included to keep the model numerically stable. In all simulations, the model was integrated for 15 model years and we show averages over the last five years of the simulations.

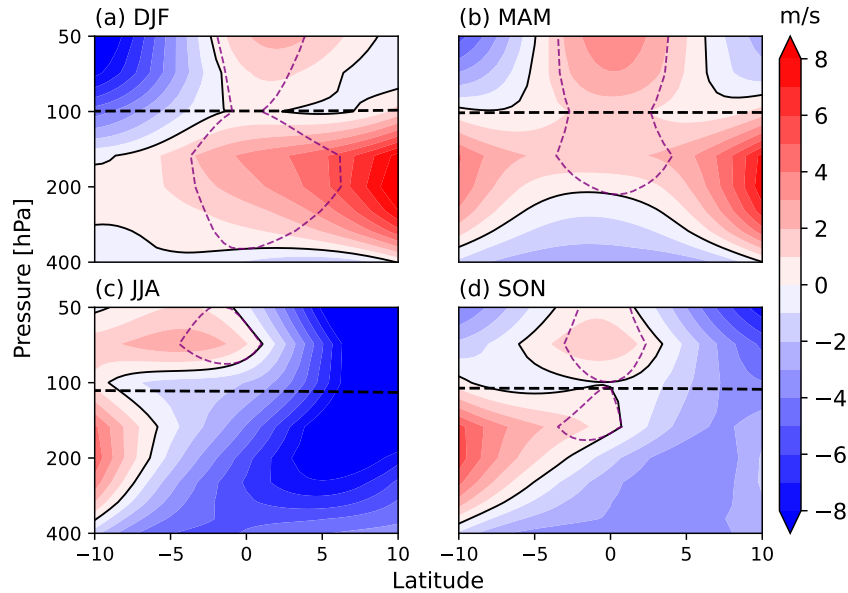
### 3. Characterizing Boreal Winter Superrotation

#### *a. Observed structure of the superrotation*

We begin by examining the spatial and temporal structure of the zonal winds near the equator. Plotting the climatological seasonal zonal-mean winds in the deep tropics clearly shows the presence of tropospheric superrotating winds in boreal winter (December, January, and February, or DJF), and also weak superrotation in March, April, and May (MAM) and September, October, and November (SON; see panels a, b and d of Figure 1). In DJF the winds over the equator are westerly between roughly 250 and 100 hPa, with a maximum speed of  $4 \text{ m s}^{-1}$  at 150 hPa. These westerly winds appear as an extension of the subtropical jet in the Northern Hemisphere, and the

171 zonal winds strengthen moving northwards from the equator. The weaker superrotation in MAM  
 172 has a maximum wind speed of less than  $2\text{ m s}^{-1}$  and is centered in a narrower band of the upper-  
 173 troposphere ( $\sim 200\text{-}100\text{ hPa}$ ). The zonal winds are more symmetric about the equator in MAM,  
 174 and there are subtropical jets in both hemispheres. The superrotation in MAM also appears to be  
 175 connected to the superrotating winds in the stratosphere, and we return to the connection between  
 176 tropospheric superrotation and the QBO below. Note that the westerlies above the tropopause are  
 177 not sensitive to the number of years included in the analysis, provided the time-series includes  
 178 enough QBO cycles; e.g., we find qualitatively similar results using 39, 40 or 41 years of data.

179 By contrast, the zonal winds do not exhibit tropospheric superrotation in boreal summer, and  
 180 there are strong easterly winds in June, July, and August (JJA). In both JJA and SON there is  
 181 a subtropical jet in the Southern Hemisphere, though this jet is not as strong as the Northern  
 182 Hemispheric subtropical jet in DJF and MAM.



183 FIG. 1. Seasonality of the tropical zonal-mean zonal wind speeds at different latitudes and levels in the  
 184 MERRA-2 reanalysis. The shading denotes wind velocities, with a contour interval of 1 m/s. The black dashed  
 185 lines denote the average height of the tropopause, defined as the lowest level at which the lapse rate decreases to  
 186 2 K/km or less. Regions where the wind speed is greater than or equal to the superrotating winds defined by Eq.  
 187 1 are enclosed by the purple dashed lines.

Figure 2 shows the meridional and zonal variations of the equatorial zonal wind at 150hPa, where the superrotation is strongest, as a function of month and latitude in (a) and month and longitude in (b). The zonal mean superrotation is established in late October and reaches its peak strength in December (Figure 2a), with a maximum speed of  $4 \text{ m s}^{-1}$ . The winds decelerate slightly in January and February, before accelerating again in March, to reach a second peak in April of  $\sim 3 \text{ m s}^{-1}$ . Seasonal subtropical westerly jets are observed in the Northern and Southern Hemispheres, and the superrotation acts to connect the two jets when both subtropical westerly jets are present. During the rest of the year, there are strong easterly winds over the equator, associated with an easterly jet in the Northern Hemisphere. The maximum easterly equatorial wind speeds are roughly  $7 \text{ m s}^{-1}$ , stronger than the superrotating winds in other seasons, and result in the annual-mean equatorial winds being easterly (this was also noted by Zurita-Gotor (2019)). In boreal winter there is a weak easterly jet in the Southern Hemisphere, which does not extend across the equator into the Northern Hemisphere.

Figure 2b gives a sense of the horizontal structure of the superrotation. A dipole pattern is observed in all seasons, with westerly winds over the tropical Atlantic ( $0^\circ$  to  $40^\circ\text{W}$ ) and eastern tropical Pacific ( $80^\circ\text{W}$  to  $180^\circ$ ), and easterly winds over the Indian Ocean and the western Pacific Ocean ( $40^\circ\text{E}$  to  $140^\circ\text{E}$ ). The westerly winds are strongest in boreal winter and spring, while the easterly winds are strongest in boreal summer, with a secondary maximum in January and February. Both the easterly and the westerly winds are weak in the spring and autumn. Hence the seasonal superrotation seems to be related to variations in the zonal overturning circulations (Walker cells) over the tropical Atlantic and eastern Pacific, as well as to the summer monsoon circulations. However, our focus in this study is on the structure of the zonal-mean superrotation, and we leave the connection to regional circulations for future work.

#### *b. Relationships with modes of climate variability*

We now investigate the superrotation's relationships with the two primary modes of interannual variability in the tropics: the El Niño Southern Oscillation (ENSO) and the Quasi-Biennial Oscillation (QBO) in the stratosphere.

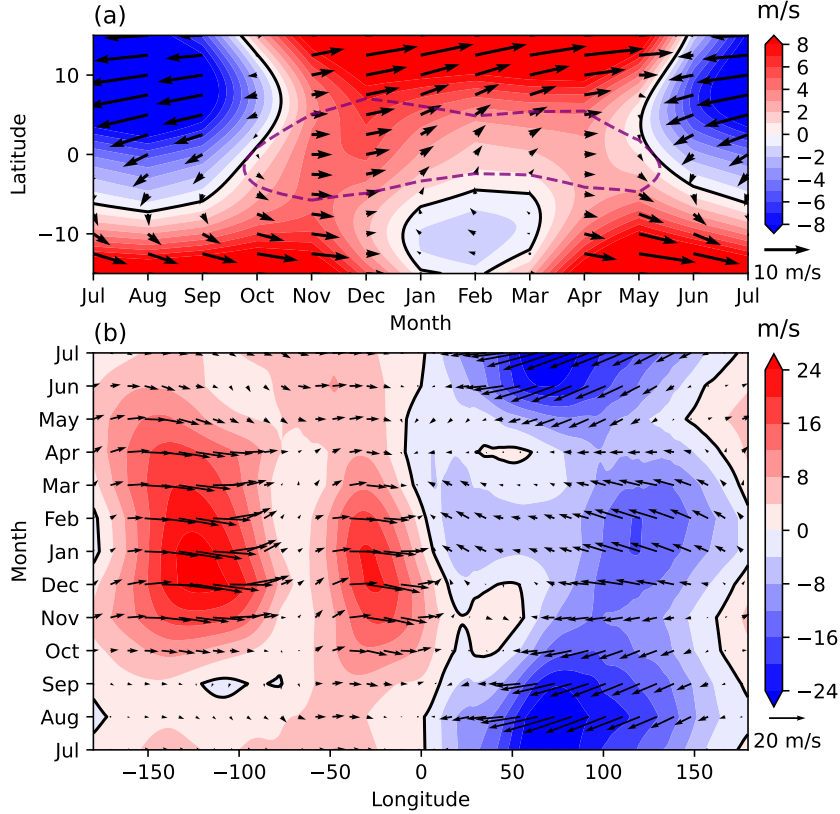


FIG. 2. Seasonality of the equatorial zonal wind speed and horizontal wind velocity direction at 150 hPa in the MERRA-2 reanalysis. (a) The zonal mean and (b) the meridional mean between 5°S to 5°N. The shading denotes zonal wind speeds; the arrows give a sense of the strength and direction of the winds; and the contour intervals are 1 m/s and 4 m/s in panels (a) and (b), respectively.

## 1) ENSO

The ENSO cycle has a strong influence on tropical stationary waves, through its modulation of tropical convection (Adames and Wallace 2017). Since stationary waves are an important part of the equatorial momentum budget, we expect in turn that ENSO should have an impact on the seasonal superrotation.

Regressing the equatorial zonal-mean zonal winds at different levels and months onto the ONI index shows a robust relationship between the tropospheric superrotation and ENSO (Table 2). In the first three months of superrotation (October, November and December, which are also the developing and mature phases of ENSO evolution), the regression coefficients are significantly

level (hPa)	Jan	Feb	Mar	Apr	May	Jun	Jul	Aug	Sep	Oct	Nov	Dec
100	<b>0.756</b>	0.102	<b>0.981</b>	<b>0.977</b>	1.140	1.080	0.364	0.062	0.143	-0.187	-0.069	-0.390
150	0.527	-0.359	-0.328	-0.944	-0.301	0.666	0.905	0.852	0.334	<b>-1.128</b>	<b>-1.205</b>	<b>-0.945</b>
200	0.146	-0.269	-0.269	-0.822	-0.287	0.525	0.733	<b>1.096</b>	0.440	<b>-0.962</b>	<b>-1.183</b>	<b>-0.719</b>

TABLE 2. Regression coefficients of the zonal mean zonal wind onto the ENSO index (ONI). The units are  $\text{m s}^{-1} \text{K}^{-1}$ , the first column shows the vertical level in pressure (hPa), and the bold numbers are coefficients that are statistically significant at the 95% confidence level passing Student's t-test.

negative at 150 and 200 hPa, as the superrotation tends to be stronger in La Niña years and weaker in El Niño years. There is an interesting contrast with Tziperman and Farrell (2009), who linked surface superrotation to the possible “permanent El Niño-like” Pacific in the early Pliocene, though we note that here the superrotation is confined to the upper troposphere rather than reaching down to the surface. We believe the mechanisms are likely to be quite different in the two cases.

Figure 3a further clarifies the relationship between the equatorial upper tropospheric zonal winds and ENSO by showing the correlation coefficients between the deseasonalized monthly zonal-mean zonal wind anomalies and the ONI. Statistically-significant negative correlations are seen throughout the mid- and upper-troposphere ( $\sim 500$ -125 hPa) in a narrow band of latitudes between  $5^\circ\text{S}$  and  $5^\circ\text{N}$ . Positive correlations are seen outside these latitudes, as the subtropical jets tend to shift equatorward in both hemispheres during El Niño years (Manney et al. 2021). The stratospheric winds in the deep tropics show a weak positive correlation with the ONI.

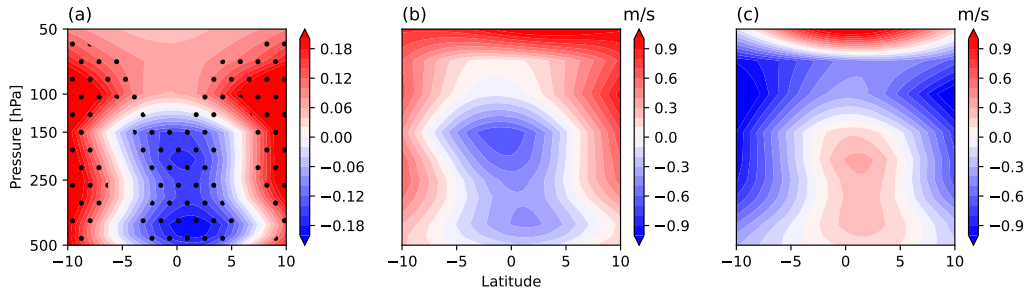


FIG. 3. (a) Correlation coefficients between the deseasonalized zonal-mean monthly zonal wind and the ONI. Stippling marks the regions where the correlation coefficients are statistically significant at the 95% confidence level, using a Student's t-test. (b) Average of deseasonalized zonal-mean monthly zonal winds in strong El Niño months ( $\text{ONI} \geq 0.6$ ); (c) Same as in (b) but for strong La Niña months ( $\text{ONI} \leq -0.6$ ).

Panels b and c of Figure 3 show the average deseasonalized zonal-mean zonal winds in strong El Niño ( $\text{ONI} \geq 0.6$ ) and strong La Niña ( $\text{ONI} \leq -0.6$ ) months, respectively. Strong El Niño months are associated with decelerations of up to  $-0.5 \text{ ms}^{-1}$  in the equatorial upper troposphere, while strong La Niña months show smaller accelerations of up to  $0.3 \text{ ms}^{-1}$ . We show in the next section that the two ENSO phases produce similar magnitude anomalies in the momentum budget (see Figure 8) despite the different strengths of the wind speed responses, suggesting either sampling error or a non-linearity in the superrotation's response to ENSO. Interestingly, the maximum acceleration during strong La Niña events occurs at slightly lower levels than the maximum deceleration during El Niño months ( $\sim 200 \text{ hPa}$  versus  $150 \text{ hPa}$ ), which may be related to the lower tropopause height during La Niña years (Liou and Ravindra Babu 2020).

## 2) QBO

The westerly phase of the QBO corresponds to a state of stratospheric superrotation, which could be related to the tropospheric superrotation investigated here. Furthermore, Figure 1 shows that the tropospheric superrotation is not well separated from the stratosphere, particularly in boreal spring. So it is possible that the two phenomena are related.

To check whether this is the case, Figure 4a shows a Hovmöller plot of the zonal-mean zonal winds in the lower stratosphere and upper troposphere of the deep tropics. The quasi-biannual cycle of the QBO is clearly visible, as is the annual cycle of the tropospheric superrotation. Tropospheric superrotation can occur during the easterly (e.g., 2019), the westerly (e.g., 2018), or even the transition phase (e.g., 2015) of the QBO, suggesting that the QBO is not its primary driver. We have confirmed this by calculating the power spectra of the winds in the upper troposphere and the lower stratosphere (not shown), and find that most of the variability in the lower stratospheric is confined to a 28-month period cycle, whereas the upper tropospheric wind's variability peaks at annual and semi-annual frequencies.

Nevertheless, when we calculate the average deseasonalized equatorial zonal winds in strong positive and negative QBO phases (defined as the magnitude of the equatorial zonal wind speed at  $50 \text{ hPa}$  being greater than  $10 \text{ ms}^{-1}$ ), there are substantial differences (Figure 4b and c). During the positive phase of the QBO, the averaged deseasonalized winds tend to be easterly in the upper troposphere, despite the strong westerly wind in the stratosphere; conversely, during the negative

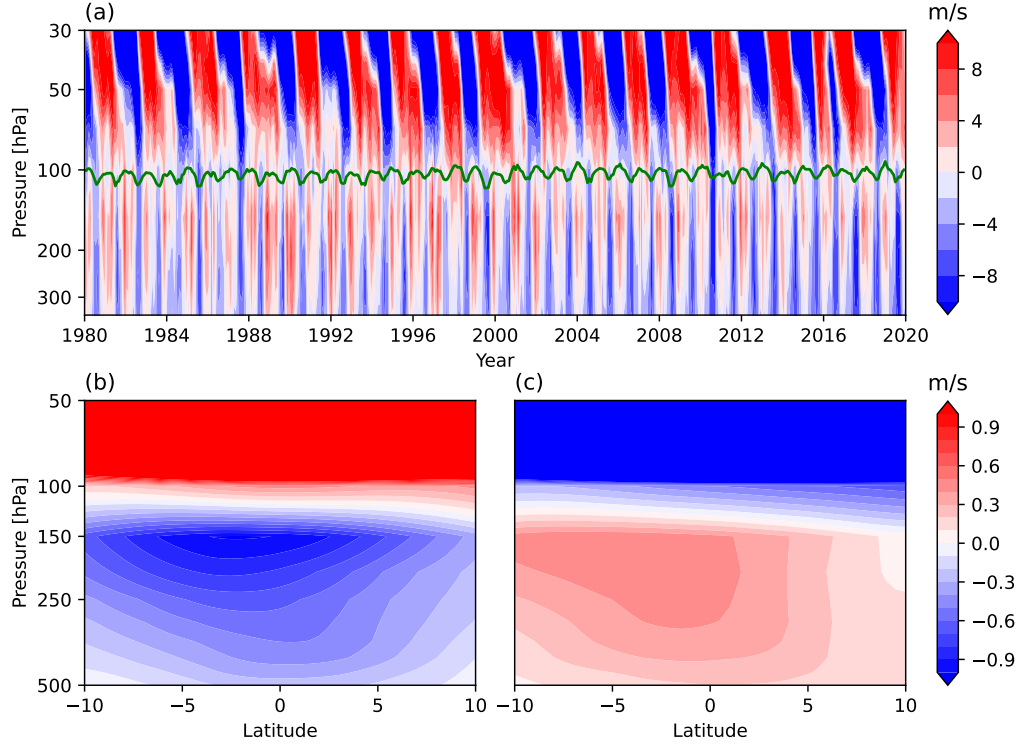


FIG. 4. (a) Zonal-mean zonal winds averaged between 5°S to 5°N in the MERRA-2 reanalysis. The green line denotes the average height of the tropopause, calculated as in Figure 2a. (b) Average of deseasonalized zonal-mean monthly zonal wind as in Figure 3b, but for strong positive QBO phase (zonal wind in (a) at 50 hPa is greater than  $10 \text{ ms}^{-1}$ ). (c) Same as in (b) but for strong negative QBO phase (zonal wind at 50 hPa in (a) is less than  $-10 \text{ ms}^{-1}$ ).

phase of QBO the deseasonalized upper tropospheric winds tend to be westerly. The contribution of the QBO to the upper tropospheric winds is comparable to that of ENSO in terms of magnitude and extends over a broader range of latitudes, including beyond the superrotation latitudes. To understand the sharp contrast between the stratospheric and upper tropospheric winds in Figure 4b and c, we have examined the Fourier components of these winds corresponding to a frequency of 28 months (not shown). Although most of the QBO signal dissipates before reaching the tropopause, a small part of the energy does penetrate below the tropopause and propagates downwards slowly. The propagating time from 50 hPa to 150 hPa is roughly half of the QBO period, such that the QBO's impact on the upper tropospheric winds is out of phase with its impact on the lower

290 stratospheric winds. We also note that the QBO is driven by upwelling gravity waves, such that  
291 the seasonal superrotation may actually be modulating the QBO.

292 Despite the influence of the downwelling QBO on the tropospheric superrotation, the seasonal  
293 signal is much larger than the contribution by the QBO (or by ENSO) and produces the consistent  
294 annual cycle of the winds in the tropical upper troposphere. The variability coming from the  
295 stratosphere is submerged by the intrinsic variability of tropospheric superrotation, and hence we  
296 treat the seasonal superrotation in the upper troposphere as a distinct phenomenon from the QBO  
297 in the following discussion of its dynamics.

### 298 *c. Observed trends*

299 We finish characterizing the observed tropospheric superrotation by examining recent trends.  
300 Table 3 shows the linear trends of the equatorial zonal-mean zonal wind at different pressure levels.  
301 Since 1980, the annual-mean equatorial zonal winds exhibit easterly trends at 150 and 200 hPa  
302 of roughly  $-0.7 \text{ m s}^{-1}/\text{decade}$ , suggesting that the superrotation has been weakening. However,  
303 when the trends are broken down by month we find that the zonal winds exhibit significant easterly  
304 trends only in boreal summer (and late spring and early autumn) months, when the winds are not  
305 superrotating.

306 Hence, although the equatorial zonal winds are decelerating in the annual-mean, the superrotation  
307 itself has been roughly constant, except in its starting and ending months. Examining the spatial  
308 structure of the trends of monthly equatorial zonal winds further reveals that the upper troposphere  
309 is decelerating throughout the tropics, with the maximum deceleration over the equator between  
310 150 and 200 hPa (Figure 5). The deceleration extends over a broader range of latitudes and heights  
311 than the superrotation (see Figure 1), suggesting that it is driven by different mechanisms.

## 319 **4. The Tropical Zonal Momentum Budget**

320 The zonal-mean zonal momentum budget of the tropical upper troposphere can be written as  
321 (Kraucunas and Hartmann 2005; Lutsko 2017):

level (hPa)	All	Jan	Feb	Mar	Apr	May	Jun	Jul	Aug	Sep	Oct	Nov	Dec
100	-0.109	-0.182	-0.225	0.417	0.322	0.331	<b>-0.862</b>	<b>-0.940</b>	<b>-0.742</b>	0.024	0.367	0.371	-0.259
150	<b>-0.721</b>	-0.270	-0.396	-0.441	-0.389	<b>-0.644</b>	<b>-1.883</b>	<b>-1.467</b>	<b>-1.881</b>	<b>-1.028</b>	0.211	-0.011	-0.623
200	<b>-0.724</b>	-0.302	-0.392	<b>-0.865</b>	<b>-0.712</b>	<b>-0.818</b>	<b>-1.834</b>	<b>-1.287</b>	<b>-1.599</b>	<b>-0.806</b>	0.211	0.091	-0.543

TABLE 3. Linear trends of the equatorial zonal winds (second column) and of January-only, February only,  $\dots$ , December-only zonal winds (rightmost 12 columns) during the period 1980-2020. The units are  $\text{m s}^{-1}/\text{dec}$ , the first column shows the vertical level in pressure (hPa), and the bold numbers are coefficients that are statistically significant at the 95% confidence level passing Student's t-test.

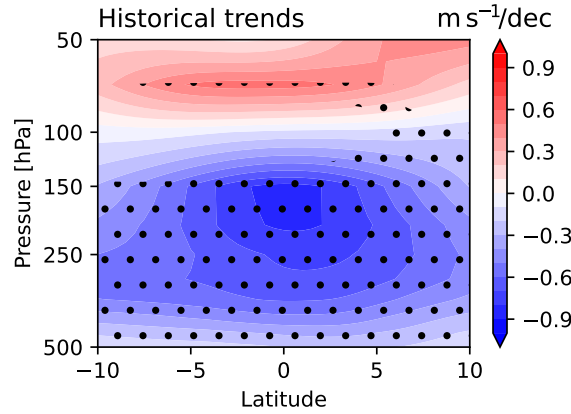


FIG. 5. Linear trends of the deseasonalized zonal-mean zonal winds over the period 1980-2020 as a function of pressure and latitude. The contour interval is  $0.1 \text{ m s}^{-1}$  per decade and stippling marks the regions where trend coefficients are statistically significant at the 95% confidence level, using a Student's t-test.

$$\begin{aligned}
\frac{\partial [\bar{u}]}{\partial t} = & f[\bar{v}] - \frac{[\bar{v}]}{a \cos \phi} \frac{\partial}{\partial \phi} ([\bar{u}] \cos \phi) - [\bar{\omega}] \frac{\partial [\bar{u}]}{\partial p} - \frac{1}{a \cos^2 \phi} \frac{\partial}{\partial \phi} ([\bar{u}^* \bar{v}^*] \cos^2 \phi) - \frac{\partial}{\partial p} [\bar{u}^* \bar{\omega}^*] \\
& - \frac{1}{a \cos^2 \phi} \frac{\partial}{\partial \phi} ([\bar{u}' v'] \cos^2 \phi) - \frac{\partial}{\partial p} [\bar{u}' \omega'] + [\bar{F}_x],
\end{aligned} \tag{7}$$

where  $[\cdot]$  denotes a zonal mean,  $\bar{\cdot}$  denotes a temporal mean,  $\cdot^*$  denotes a departure from the zonal mean and  $\cdot'$  is a departure from the temporal mean.  $a$  is the Earth's radius,  $F_x$  is the zonal frictional drag and  $f$  is the Coriolis parameter. Other notation is standard.

As in Lutsko (2017), we refer to the second and third terms on the RHS as the mean horizontal and the mean vertical terms, respectively; the fourth and fifth terms as the stationary horizontal and

stationary vertical terms, respectively; and the sixth and seventh terms as the transient horizontal and transient vertical terms, respectively. The frictional term is small in the free troposphere, so we have not calculated it explicitly. We have used daily-mean data to calculate the momentum budget, so momentum transport by higher frequency waves is included in the residual.

#### *a. Monthly zonal-mean zonal momentum budgets*

In order to understand the dynamics of the superrotation, we have calculated the monthly-mean zonal-mean zonal momentum budget using Eq. 7. Time-means represent monthly averages and transient eddies are calculated as departures from the monthly average. Each term in Eq. 7 is calculated for individual months, and the climatological monthly average is obtained to show the seasonal evolution of the terms in the budget.

The stationary horizontal term, which represents the momentum flux convergence by horizontal stationary eddies, is the only term accelerating the zonal equatorial flow (Figure 6). This acceleration is centered at around 150 hPa, extends between roughly 300 hPa and 100 hPa, and matches the vertical structure of the superrotation. Dima et al. (2005) also showed that the upper tropospheric stationary waves are strongest near the 150 hPa level, consistent with the vertical position of superrotation. Further away from the equator, there are two regions of deceleration by stationary waves in each hemisphere. This is analogous to the momentum transport at mid-latitudes, where Rossby waves transport momentum from wave sinks to sources (Thompson 1971; Hide and Mason 1975), and suggests the presence of wave sources close to the equator. One likely driver of tropical stationary waves is deep convection, for example in the Indo-Pacific Warm Pool. This convection is part of the Walker circulation, and both the superrotation and the Walker circulation are stronger in La Niña than in El Niño years. We will come back to ENSO’s influence on the momentum budget later in this section.

The location of the maximum acceleration by the stationary horizontal term varies over the course of the year, from just north of the equator in boreal summer to just south of the equator in boreal winter. This shift corresponds to the north-south migration of the ITCZ, and suggests the stationary wave source shifts with the ITCZ. The strength of the acceleration shows a semi-annual cycle: the acceleration is largest in boreal winter, then decays until its contribution in the deep tropics is negligible in May; in the boreal summer another peak is observed, and then the stationary

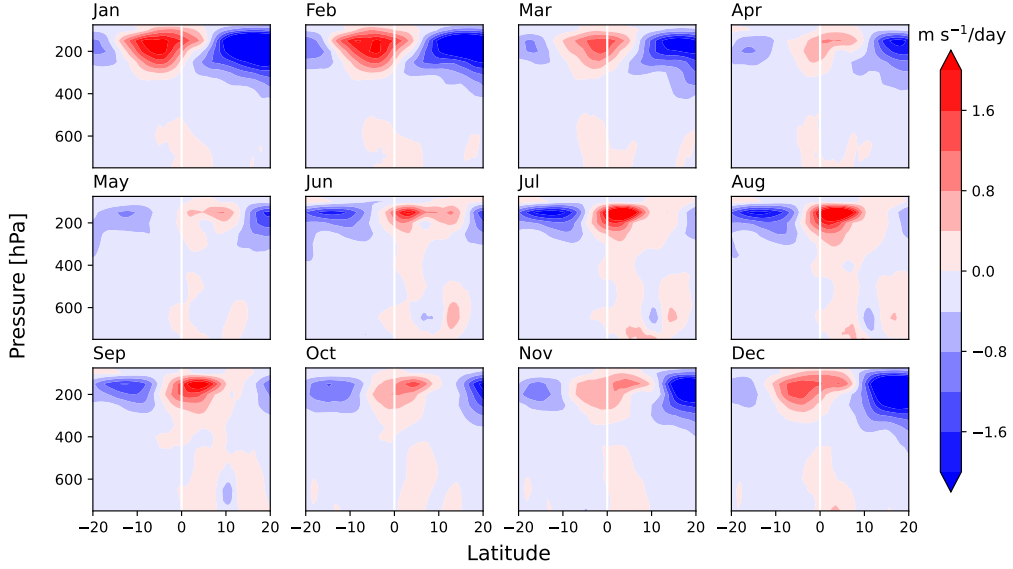


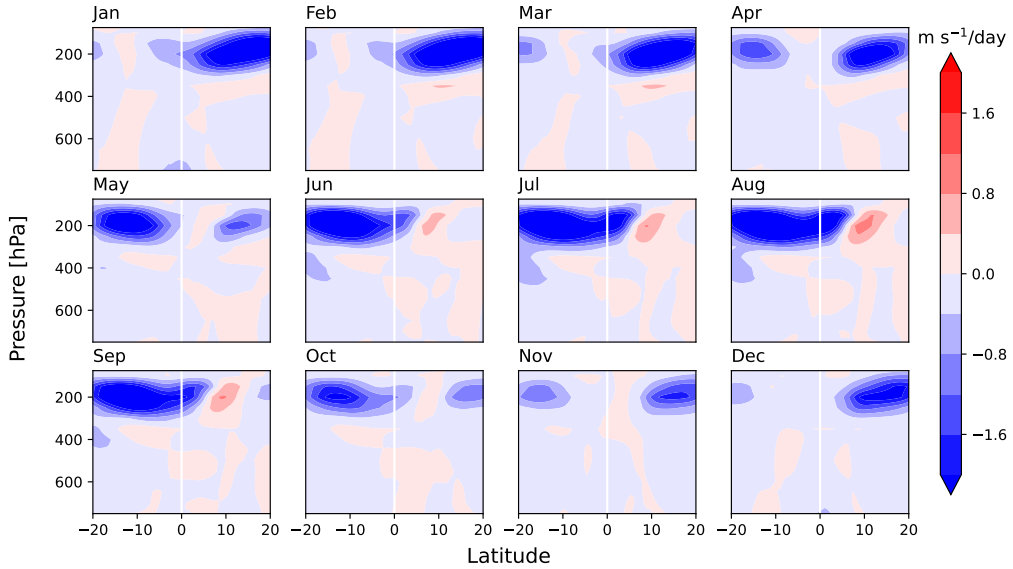
FIG. 6. Seasonal evolution of the monthly stationary horizontal term in Eq. 7 as a function of latitude and pressure. The contour interval is  $0.4 \text{ m s}^{-1}/\text{day}$  in all panels.

horizontal acceleration decays again in the autumn. The winter peak of the eddy momentum flux convergence coincides with the period of superrotation but, unlike the superrotation, the stationary horizontal term also peaks in boreal summer. The boreal summer peak is weaker than the boreal winter peak.

Off the equator, the two regions of deceleration by stationary waves also exhibit an annual cycle, with the deceleration stronger in the winter hemisphere than in the summer hemisphere, consistent with Kraucunas and Hartmann (2005). Moreover, the winter deceleration in the subtropics is stronger in DJF (boreal winter) than in JJA (austral winter), which matches the finding of Schneider and Bordonì (2008) that the winter overturning cell in boreal summer is angular momentum conserving, whereas in DJF the winter cell is primarily eddy dominated.

The major deceleration of equatorial flow is induced by the mean horizontal term. In the monthly budget, this term represents the transport of air with low angular momentum across the equator by the mean meridional flow associated with the seasonal Hadley cells. The importance of deceleration by the mean flow is consistent with Lee (1999) and Dima et al. (2005), who concluded that the most significant factor stopping the tropics from superrotating in the annual-mean is the

373 “transient” meridional circulation associated with the seasonal cycles of the Hadley cells, though  
 374 the transience of the Hadley cells in their studies is categorized as a mean flow effect in our monthly  
 375 budget. Mitchell et al. (2014) also showed that even a relatively weak seasonal cycle effectively  
 376 prevents model atmospheres from developing superrotation.



377 FIG. 7. Seasonal cycle of the monthly mean horizontal term in Eq. 7 as a function of latitude and pressure.  
 378 The contour interval is  $0.4 \text{ m s}^{-1}/\text{day}$  in all panels.

379 Figure 7 shows the annual cycle of the mean horizontal term. The deceleration is strongest in  
 380 boreal winter and summer when the cross-equatorial meridional flow is strong, and weakest in  
 381 spring and autumn when the Hadley cells are roughly symmetric and the cross-equatorial flow is  
 382 weak. The strong deceleration in boreal summer – even stronger than in boreal winter – explains  
 383 why the winds do not superrotate in that season despite the substantial acceleration by stationary  
 384 eddies. This is consistent with the differing strength of the winter Hadley cells: stronger in austral  
 385 winter than in boreal winter, reflecting the northward displacement of ITCZ from the equator in  
 386 the annual mean. We will further discuss the effect of the displaced annual-mean ITCZ in section  
 387 5.

388 Together, the mean horizontal term and the mean stationary term largely explain the superrotation,  
 389 and more generally, the seasonal evolution of the upper tropospheric winds in the tropics (see also

Zurita-Gotor 2019). Other terms in the momentum budget, such as the vertical terms and transient horizontal term, play minor roles in the monthly momentum budget of the deep tropics (not shown), though they may be important in other contexts (e.g., the vertical momentum flux can be crucial when superrotation becomes much stronger, as in Kraucunas and Hartmann 2005, for example).

Putting these results together shows that superrotation of the upper troposphere can only develop outside the boreal summer months, when the deceleration by the mean flow is relatively weak and cannot overcome the acceleration by the stationary waves. Even in autumn and spring, when the stationary momentum convergence is weak, the mean flow deceleration is unable to inhibit the superrotation. But in boreal summer, the strong cross-equatorial flow decelerates the zonal-mean winds so strongly that in the annual-mean the zonal-mean winds are easterly.

### *b. Influences of ENSO and QBO*

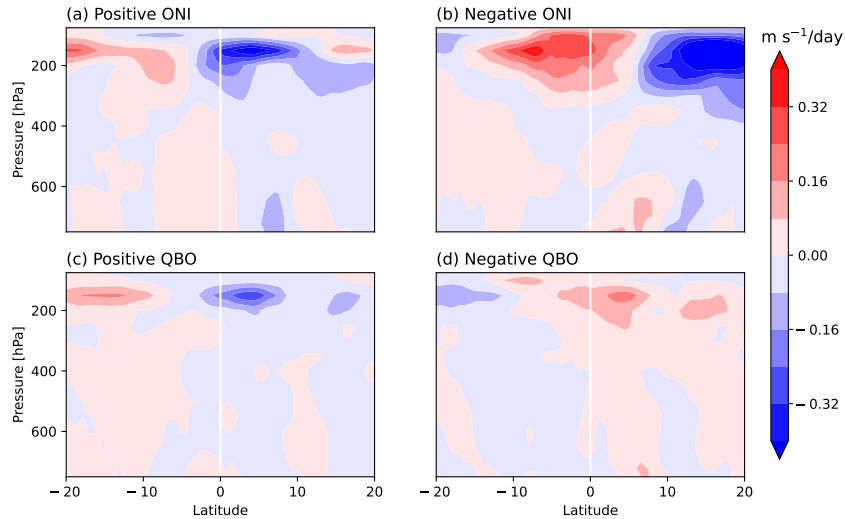
In Section 3, the ENSO and the QBO were shown to have notable influences on the strength of superrotation, which suggests that they impact the stationary eddy momentum convergence that drives the superrotation. To explore this possibility, we have averaged the anomalous monthly stationary horizontal term (deviations from the climatological monthly mean) over strong El Niño months ( $\text{ONI} \geq 0.6$ , 111 months) and strong La Niña months ( $\text{ONI} \leq -0.6$ , 107 months), as well as over strong positive and negative QBO months (Figure 8, 161 and 119 months, respectively). Note that other terms, such as the mean horizontal and vertical terms, are weakly correlated to ENSO and to the QBO (not shown), suggesting that both modes of variability primarily influence the momentum budget through changes in stationary waves.

For ENSO, the anomalous stationary horizontal term is negative over the equator between 300 hPa and 100 hPa during strong El Niño months and positive during strong La Niña months (Figure 8a and b), as the momentum convergence by stationary eddies becomes weaker in El Niño years and stronger in La Niña years<sup>4</sup>. This explains why the superrotation is stronger in La Niña years and weaker in El Niño years, though, interestingly, the magnitude of the anomalous stationary horizontal term is similar during El Niño and La Niña months, whereas the wind response is stronger during El Niño than La Niña (Figure 3). This could be the result of sampling bias or of a nonlinear mechanism by which ENSO modifies the superrotation.

---

<sup>4</sup>See Adames and Wallace (2017) for a discussion of how stationary waves change over the course of the ENSO cycle; Dima and Wallace (2007) and Grise and Thompson (2012) also suggested enhanced amplitudes of the equatorial planetary waves associated with “La Niña-like” SST anomalies, which are perhaps induced by modulation of tropical convection.

418 The QBO modifies the equatorial momentum convergence in the region of superrotation in a  
 419 similar manner to ENSO (Figure 8c and d). Note that the anomalies are stronger in positive QBO  
 420 than in negative QBO phases, consistent with the differing strengths of the wind responses to QBO  
 421 phases (Figure 4). We have not investigated the stationary wave response to the QBO further, but  
 422 note that Yang et al. (2012) found that the upper-tropospheric planetary waves over the eastern  
 423 Pacific region appear to be stronger during the easterly phase, and Collimore et al. (2003) and  
 424 Yamazaki et al. (2020) also suggested that the easterly phase enhances deep convection in the  
 425 tropical western Pacific. Investigating the couplings between the QBO, the winds of the tropical  
 426 upper troposphere and tropical stationary waves, all of which modify and are modified by each  
 427 other, could be a fruitful topic of future research.



428 FIG. 8. Upper row: Anomalous monthly stationary horizontal term, (a) in strong El Niño months ( $\text{ONI} \geq 0.6$ )  
 429 and (b) in strong La Niña months ( $\text{ONI} \leq -0.6$ ). Bottom row: as in upper row but for (c) positive QBO months  
 430 (equatorial zonal-mean zonal wind is greater than  $10 \text{ m s}^{-1}$ ) and (d) negative QBO months (equatorial zonal-mean  
 431 zonal wind is less than  $-10 \text{ m s}^{-1}$ ).

## 432 5. Understanding the Superrotation with an Idealized Model

433 The previous section showed how stationary momentum flux convergence and deceleration by  
 434 the mean flow combine to produce the observed seasonal cycle of winds in the tropical upper  
 435 troposphere. The northward displaced ITCZ also appears to play a role in setting the seasonal

cycle of the superrotation. We now use an axisymmetric single-layer model to further understand the dynamics and seasonal development of the superrotation. We also verify our arguments from the momentum budget analysis, and separately show the effects of the stationary eddy momentum flux convergence and the displacement of the ITCZ.

We consider four model configurations: (1) no Eddy Momentum Flux Divergence (EMFD,  $\mathcal{S}$  in Eq. 2) and hemispherically-symmetric insolation; (2) no EMFD but hemispherically-asymmetric insolation; (3) prescribed EMFD and hemispherically-symmetric insolation; (4) prescribed EMFD and hemispherically-asymmetric insolation. The purpose of hemispherically-asymmetric insolation is to match the observed northward displacement of the ITCZ in the annual-mean. The prescribed EMFD is based on the stationary horizontal terms described in the previous section, and takes the following form:

$$\mathcal{S} = \begin{cases} -2.4N(0,3) + 2.4N(15,3) + 0.1N(-15,3) & \text{if } d < 60 \text{ or } d > 285, \\ -2.2N(0,3) + 1.3N(15,3) + 1.3N(-15,3) & \text{if } d > 155 \text{ and } d < 260, \\ -1.3N(0,3) + 0.5N(15,3) + 0.5N(-15,3) & \text{otherwise.} \end{cases} \quad (8)$$

where the units are  $10^{-6} \text{ m s}^{-2}$ ,  $d$  is the day of the year, ranging from 0 to 364, and  $N(0,3)$  is a Gaussian-like function centered at  $0^\circ$  with a maximum of 1 and a standard deviation of  $3^\circ/\sqrt{2}$ .  $\mathcal{S}$  is shown in Figure 9.

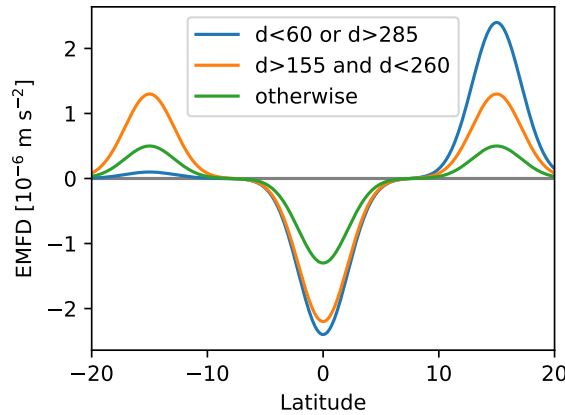


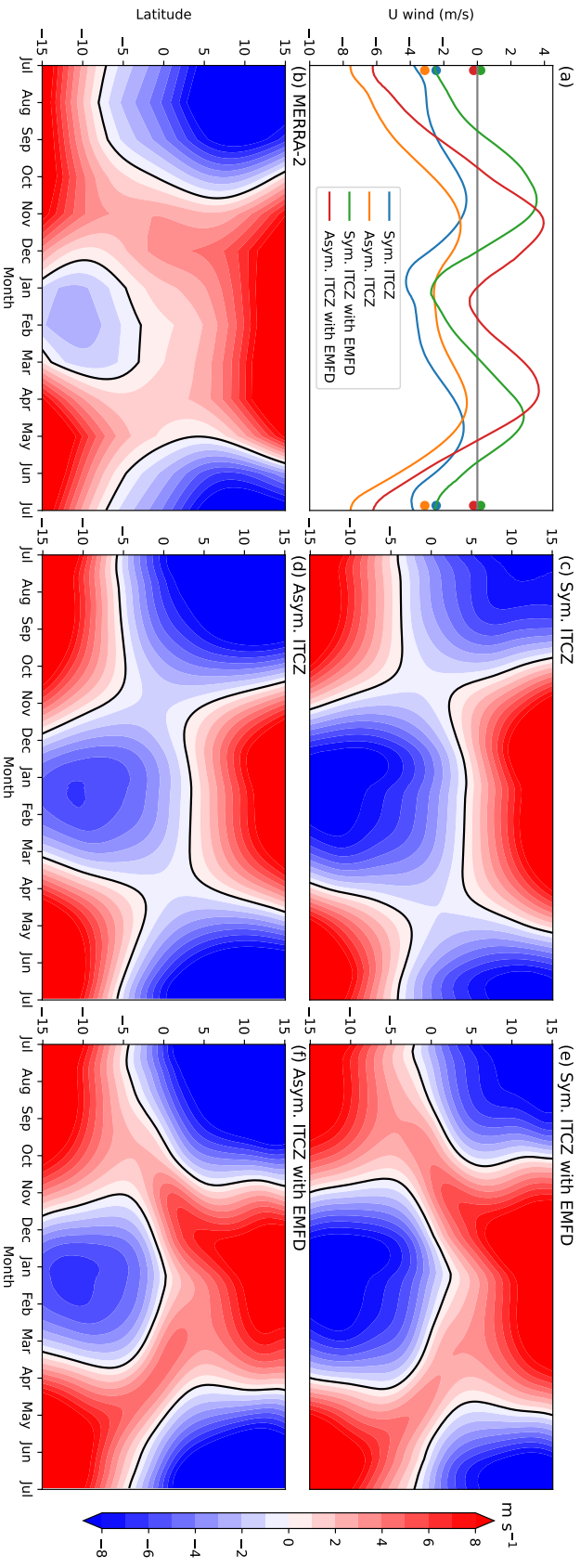
FIG. 9. Prescribed eddy momentum flux divergence in the model simulations, based on the stationary horizontal term.

452 This function captures the key features of the horizontal stationary term in the upper troposphere:  
 453 (1) peaks in boreal summer and winter; (2) weak, hemispherically-symmetric EMFD in the shoulder  
 454 seasons; and (3) strong subtropical deceleration in the Northern Hemisphere during boreal winter.  
 455 Our formulation of  $\mathcal{S}$  roughly matches the observed EMFD, but allows more freedom to adjust  
 456 the parameters and match the observations. Given the idealizations of the model and the difficulty  
 457 of constraining certain model parameters such as friction, we find it easier to prescribe an EMFD  
 458 that can be tuned so that the model matches the observations. Moreover, the simulation results, in  
 459 terms of the key feature of superrotation, are qualitatively robust to the choice of  $\mathcal{S}$  (not shown).

460 With this numerical model, we are able to clarify how the northward displacement of the ITCZ  
 461 and the stationary eddy momentum convergence contribute to the seasonal superrotation. We  
 462 begin with the simplest case of an ITCZ that is symmetric about the equator and with no eddy  
 463 momentum convergence input. Figure 10c and the blue curve in Figure 10a show that in this case  
 464 the winds in the equatorial upper troposphere are easterly in all seasons. The easterly flow is driven  
 465 by the easterly momentum transport by the cross-equatorial mean flow of the upper branch of the  
 466 Hadley cell, which gives a semi-annual cycle in the upper tropospheric winds. The easterly winds  
 467 are weakest in spring and autumn when the ITCZ is close to the equator and the cross-equatorial  
 468 flow is weak; hence these seasons are most favorable for the development of superrotation.

474 In the second simulation the annual mean ITCZ is displaced to the Northern Hemisphere (Figure  
 475 10d and the orange curve in Figure 10a). In this case the equatorial wind has an annual rather than a  
 476 semi-annual cycle, as the easterlies substantially strengthen in boreal summer and weaken in boreal  
 477 winter, breaking the symmetry between summer and winter. This is because the cross-equatorial  
 478 flow is stronger in boreal summer, when the ITCZ is further from the equator, than in winter, when  
 479 the ITCZ is closer. A stronger easterly flow is expected for an angular-momentum conserving  
 480 Hadley Circulation that is displaced off the equator in the annual-mean (Lindzen and Hou 1988).

481 Next, we add eddy momentum flux convergence to the model. This accelerates the flow, and  
 482 drives seasonal superrotation when the cross-equatorial flow is weak in the shoulder seasons (Figure  
 483 10e and f, and the green and red curves in Figure 10a). The resulting superrotation has either an  
 484 annual cycle or a semi-annual cycle, depending on the mean ITCZ position. In the hemispherically-  
 485 symmetric case (Figure 10e and green curve in Figure 10a), the superrotation peaks in boreal spring  
 486 and autumn with almost equal strength, and completely disappears in boreal summer and winter.



469 Fig. 10. (a) The equatorial wind from the numerical model under different model configurations; winds are averaged between 3°S to 3°N and the  
 470 colored dots on the y-axis show the annual mean winds in each configuration. (b) The seasonality of the equatorial winds in the MERRA-2 reanalysis,  
 471 averaged between 100 and 200 hPa. (c-f) Seasonality and latitudinal distribution of the equatorial wind in the numerical model simulations: (c)  
 472 Symmetric ITCZ; (d) Northward displaced ITCZ; (e) Symmetric ITCZ with prescribed EMFD; and (f) Northward displaced ITCZ with prescribed  
 473 EMFD. The contour interval is 1 m/s in all panels.

487 In the displaced ITCZ case (Figure 10f and red curve in Figure 10a), the annual-mean zonal flow  
488 is decelerated because of the stronger easterlies in boreal summer. This is partially compensated  
489 by slower easterlies in boreal summer and stronger superrotation in the shoulder seasons. The time  
490 between the two westerly peaks is shortened by several months, and the upper tropospheric winds  
491 exhibit a roughly annual cycle.

492 The model simulation with prescribed EMFD and a displaced annual-mean ITCZ shows good  
493 agreement with the MERRA-2 data (Figure 10b and f). Just like the reanalysis data, the superro-  
494 tation starts in October and reaches a first peak of  $\sim 4 \text{ ms}^{-1}$  in late November. In boreal winter  
495 the superrotation decays to zero, then reaches a second peak in late March, which has almost the  
496 same strength as the first one. Finally the superrotation vanishes in late May, and after that the  
497 equatorial upper troposphere is dominated by strong easterly winds, with a maximum of more than  
498  $6 \text{ ms}^{-1}$ . As for the spatial structure, the superrotation extends the subtropical easterly jet towards  
499 the equator, as we see in Figure 10b and Figure 1. The subtropical easterlies are caused by the  
500 Coriolis force acting on the mean meridional flow in the winter hemisphere, although the driver of  
501 superrotation itself is not the Coriolis force. All these features are consistent with what is observed  
502 in the MERRA-2 reanalysis (Figure 10b, or Figure 2a).

503 There are still some differences between the model output and the MERRA-2 reanalysis, for  
504 example, the easterly wind is stronger in boreal winter and the overall amplitude of the wind is  
505 slightly higher in the model. This likely reflects the simplifications of the model, and we have also  
506 not rigorously tuned the model, so it may be possible to produce an even better fit to the data.  
507 Nevertheless, the model successfully captures the main features of the superrotation and provides  
508 several insights into its dynamics. First, the model simulations confirm that momentum transport  
509 by the meridional flow associated with the seasonal Hadley cells decelerates the upper tropospheric  
510 winds and prevents superrotation in the annual-mean (see also Lee 1999; Dima et al. 2005). The  
511 model also illustrates how this effect can be interpreted in terms of the annual-mean ITCZ being  
512 displaced off the equator. Second, the momentum convergence induced by eddies accelerates the  
513 atmosphere to reach a superrotating state when the deceleration by the meridional flow is weak in  
514 boreal winter, autumn and spring. Finally, the asymmetric ITCZ not only slows down the annual  
515 mean equatorial wind, but also breaks the temporal symmetry of the seasonal superrotation, giving  
516 it an annual, rather than semi-annual, cycle.

## 6. Conclusion

In this study, we have characterized the seasonal superrotation of Earth's tropical upper troposphere using MERRA-2 reanalysis data. We have described the structure and seasonal evolution of the superrotation, and also identified the drivers of the superrotation using the monthly zonal-mean zonal momentum budget of the tropics. A single-layer axisymmetric model was then used to study how stationary eddy momentum fluxes and the northward displacement of the annual-mean ITCZ combine to determine the superrotation's strength and annual cycle.

The tropospheric superrotation is centered at 150 hPa and has a clear annual cycle: it is established in October, reaches peaks in December and in March, and vanishes in late April. The maximum westerlies can reach up to  $4\text{ ms}^{-1}$  during the first peak in December. The equatorial upper troposphere exhibits strong easterly winds in boreal summer, such that the tropical upper troposphere does not superrotate in the annual-mean. Regressions onto the ONI ENSO index show that the superrotation tends to be stronger in boreal winter during La Niña years, and weaker during El Niño years, while the relationship with the QBO is complex. The tropospheric superrotation is clearly a distinct phenomenon from the stratospheric superrotation during the westerly phase of the QBO, but the superrotation is actually strengthened during the easterly phase of the QBO, when the westerly acceleration of the previous (westerly) QBO phase appears to descend into the upper troposphere. On the other hand, since the QBO is driven by upwelling gravity waves, the direction of causality is ambiguous. On longer time-scales, there was a negative trend in the annual-mean winds of the upper troposphere over the period 1980-2020, but the trends were negligible from October to March, so that the strength of the superrotation was roughly constant over the past few decades.

The zonal momentum budget analysis and numerical model simulations have provided insights into the dynamics of the tropospheric superrotation. Consistent with Dima et al. (2005) and Zurita-Gotor (2019), the dominant balance in the momentum equation on monthly time-scales is between momentum flux convergence by stationary eddies and easterly momentum transport by the cross-equatorial mean flow of the Hadley circulation, with the former accelerating and the latter decelerating the upper troposphere. The stationary eddy momentum flux convergence is strongest in boreal winter and summer, whereas the deceleration by the mean flow is strongest in boreal summer, which is what prevents the tropical troposphere from superrotating in boreal summer and

547 causes the winds to be easterly in the annual-mean. Lee (1999) included the seasonal cycle of  
548 the Hadley circulation in the transient term of the annual-mean momentum budget, and similarly  
549 identified this term as the main factor stopping annual-mean superrotation.

550 The numerical model further reinforced the importance of the stationary eddy momentum con-  
551 vergence for driving the superrotation; without this acceleration, the winds of the tropical upper  
552 troposphere would be easterly throughout the year. The model also revealed the importance of the  
553 northward displacement of the ITCZ in the annual-mean for determining the seasonal cycle of the  
554 superrotation. If the annual-mean ITCZ was symmetric about the equator the winds of the tropical  
555 upper troposphere would exhibit a semi-annual cycle, with periods of strong superrotation in boreal  
556 spring and autumn, and easterly winds in boreal summer and winter. Instead, the winds exhibit  
557 an annual cycle, because the deceleration by the mean flow is relatively weak in boreal winter.  
558 Even in simulations without eddy forcing, a transition between semi-annual and annual cycles is  
559 seen depending on the ITCZ's annual-mean position. Finally, we may infer that, if the Earth were  
560 to have lower obliquity, or if the annual-mean ITCZ were closer to the equator, the winds of the  
561 tropical upper troposphere would likely superrotate in the annual-mean.

562 Our focus in this study has been on the zonal-mean structure and dynamics of the superrotation.  
563 We have not attempted to characterize the structure of the stationary waves which drive the super-  
564 rotation (see Zurita-Gotor 2019), nor how these waves change during the ENSO and QBO cycles.  
565 Figure 2b further suggests that the superrotation is related to changes in the zonal overturning  
566 cells in the deep tropics (the Walker cell, etc.), and clarifying this relationship is another topic for  
567 future research. More work is also needed to investigate how the seasonal superrotation relates to  
568 intraseasonal modes of tropical variability, such as the Madden-Julian Oscillation (e.g., see Ca-  
569 ballero and Huber 2010), as well as to examine climate model projections of how the superrotation  
570 will change in the future.

*Acknowledgments.* The manuscript was much improved by constructive comments and feedback from Professor Jun Yang and other two anonymous reviewers. We thank Matt Luongo, Professor Shang-Ping Xie, and Professor Pablo Zurita-Gotor for helpful comments on earlier versions of this manuscript.

*Data availability statement.* The MERRA-2 data are available at Goddard Earth Sciences Data and Information Services Center (GES DISC, <https://doi.org/10.5067/QBZ6MG944HW0>). The ERA5 data are available at Copernicus climate data store (<https://doi.org/10.24381/cds.6860a573>). The JRA-55 data are available at GES DISC (<https://doi.org/10.5065/D60G3H5B>). The NCEP-1 data are available on NOAA's website (<https://psl.noaa.gov/data/gridded/data.ncep.reanalysis.html>). The ONI index is available on CPC website ([https://origin.cpc.ncep.noaa.gov/products/analysis\\_monitoring/ensostuff/ONI\\_v5.php](https://origin.cpc.ncep.noaa.gov/products/analysis_monitoring/ensostuff/ONI_v5.php)). The numerical model used in section 5 is publicly available at <https://github.com/zpcllyj/SobelSchneiderModel>.

## APPENDIX

### Seasonal Superrotation in Other Reanalysis Products

To verify the robustness of the seasonal superrotation, Figure A1 shows the zonal-mean zonal winds in the deep tropics of four reanalysis products: MERRA-2, ERA5, JRA-55, and NCEP-1. The first three reanalysis products show close agreement in terms of the spatial and temporal structure of the winds, despite minor differences in wind speed magnitude, but NCEP-1 does not exhibit superrotation in boreal winter (rightmost column in Figure A1), consistent with Dima et al. (2005). We have not investigated what causes the differences in NCEP-1, but note that in addition to being an older dataset, the horizontal resolution of NCEP-1 is only  $2.5^{\circ} \times 2.5^{\circ}$ , much lower than the resolutions of the three other modern reanalysis products. This lower resolution could lead to a worse representation of tropical waves, which might impact the representation of the seasonal cycle of the tropical winds.

We have also used the different reanalysis products to verify our claim that the superrotation did not exhibit meaningful trends over the period of study (1980-2020). Figure A2 shows the linear trends of the winds in the tropical upper troposphere in the three high-resolution reanalysis products: MERRA-2, ERA-5, and JRA-55. None of the datasets show a statistically significant

600 trend in DJF, when the superrotation is most pronounced, though the trends are very different in  
601 the three datasets. The trends are more consistent in the annual-mean, with a negative trend in the  
602 middle troposphere, but the magnitude and position are slightly different. This trend appears to  
603 be driven by a different mechanism than the superrotation, as the maximum deceleration is below  
604 the superrotation level and the trend is generally strongest in boreal summer, when superrotation  
605 is absent.

## 616 References

- 617 Adames, A. F., and J. M. Wallace, 2017: On the tropical atmospheric signature of El Niño. *Journal*  
618 *of the Atmospheric Sciences*, **74** (6), 1923–1939.
- 619 Arnold, N. P., E. Tziperman, and B. Farrell, 2011: Abrupt transition to strong superrotation driven  
620 by equatorial wave resonance in an idealized GCM. *Journal of the Atmospheric Sciences*, **69** (2),  
621 626–640.
- 622 Baldwin, M. P., and Coauthors, 2001: The Quasi-Biennial Oscillation. *Reviews of Geophysics*,  
623 **39** (2), 179–229.
- 624 Belton, M. J. S., and Coauthors, 1991: Images from Galileo of the Venus cloud deck. *Science*,  
625 **253** (5027), 1531–1536.
- 626 Bird, M. K., and Coauthors, 2005: The vertical profile of winds on Titan. *Nature*, **438** (7069),  
627 800–802.
- 628 Caballero, R., and M. Huber, 2010: Spontaneous transition to superrotation in warm climates  
629 simulated by CAM3. *Geophysical Research Letters*, **37** (11).
- 630 Collimore, C. C., D. W. Martin, M. H. Hitchman, A. Huesmann, and D. E. Waliser, 2003: On the  
631 relationship between the QBO and tropical deep convection. *Journal of Climate*, **16** (15), 2552  
632 – 2568.
- 633 Dahlman, L., 2016: Climate variability: Oceanic Niño Index. URL [https://www.climate.gov/](https://www.climate.gov/news-features/understanding-climate/climate-variability-oceanic-nino-index)  
634 [news-features/understanding-climate/climate-variability-oceanic-nino-index](https://www.climate.gov/news-features/understanding-climate/climate-variability-oceanic-nino-index).

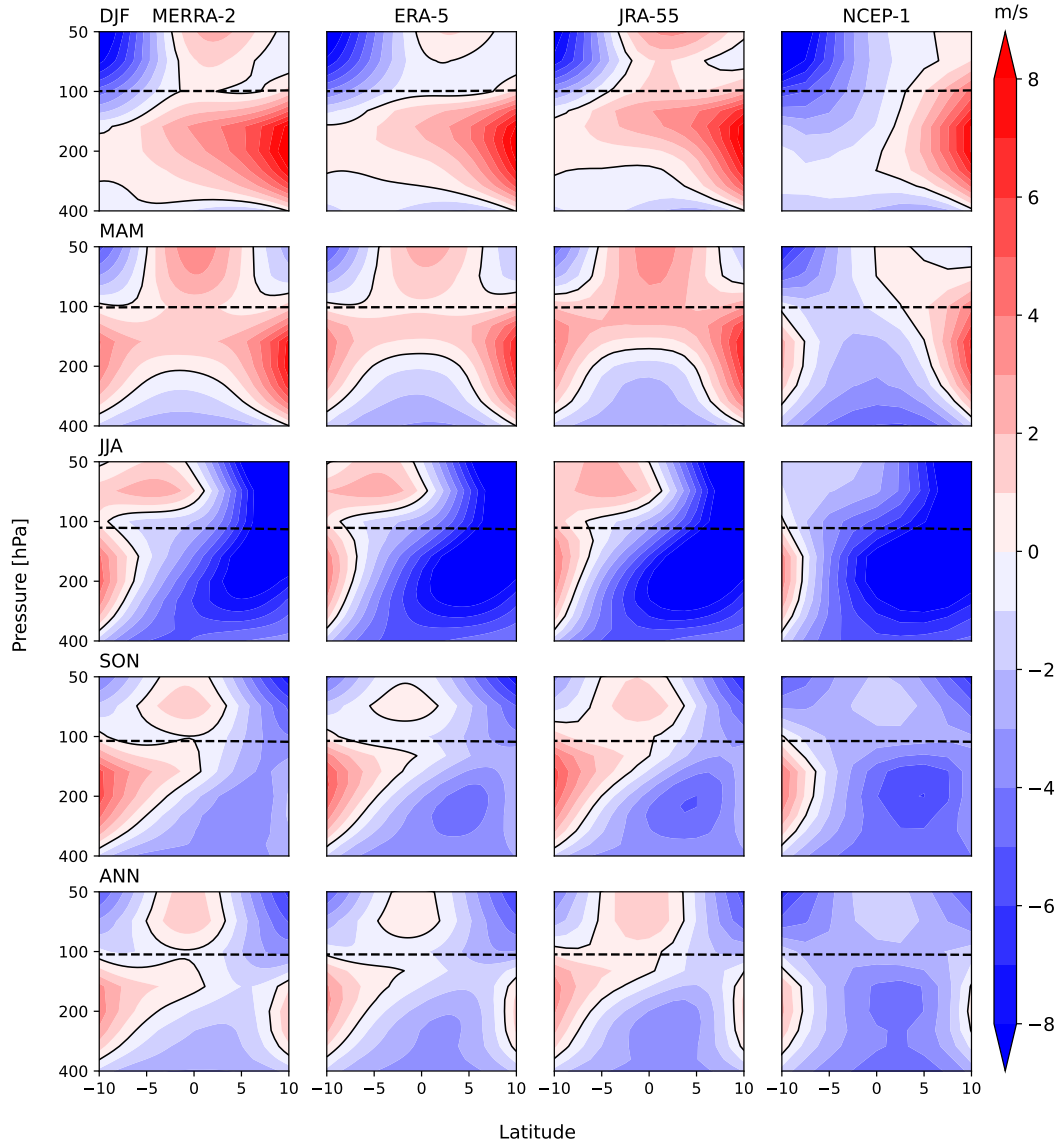


FIG. A1. Seasonality of the tropical zonal-mean zonal wind speeds at different latitudes and levels in different reanalysis products: (first column) MERRA-2, (second column) ERA-5, (third column) JRA-55, and (fourth column) NCEP-1. Five rows correspond to DJF, MAM, JJA, SON, and annual mean. The shading denotes wind velocities, with a contour interval  $1 \text{ ms}^{-1}$ . The black dashed lines denote the average height of the tropopause, defined as the lowest level at which the lapse rate decreases to  $2 \text{ K/km}$  or less.

Dima, I. M., and J. M. Wallace, 2007: Structure of the annual-mean equatorial planetary waves in the era-40 reanalyses. *Journal of the Atmospheric Sciences*, **64** (8), 2862 – 2880, <https://doi.org/10.1175/JAS3985.1>.

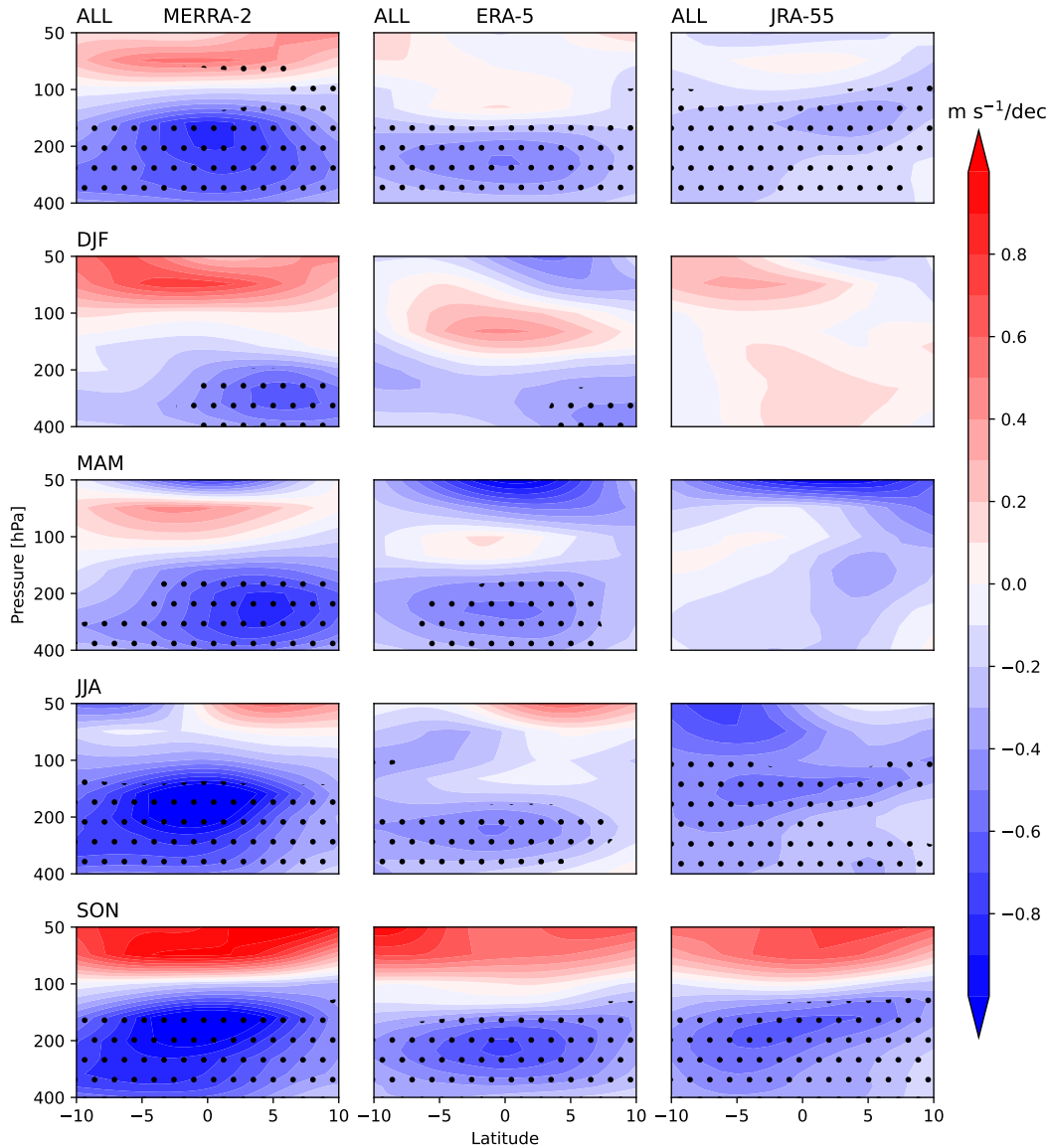


FIG. A2. Linear trends of the deseasonalized monthly zonal winds (first row) and DJF-only, MAM-only, JJA-only, and SON-only zonal winds (second to fifth rows) during the period 1980-2020 as a function of pressure and latitude in different reanalysis products: (first column) MERRA-2, (second column) ERA-5, and (third column) JRA-55. The contour interval is  $0.1 \text{ m s}^{-1}$  per decade and stippling marks the regions where trend coefficients are statistically significant at the 95% confidence level, using a Student's t-test

Dima, I. M., J. M. Wallace, and I. Kraucunas, 2005: Tropical zonal momentum balance in the NCEP Reanalyses. *Journal of the Atmospheric Sciences*, **62** (7), 2499–2513.

640 Eliassen, A., and E. Kleinschmidt, 1957: *Dynamic Meteorology*, 64–72. Springer Berlin Heidelberg,  
641 berg, Berlin, Heidelberg, [https://doi.org/10.1007/978-3-642-45881-1\\_1](https://doi.org/10.1007/978-3-642-45881-1_1), URL [https://doi.org/](https://doi.org/10.1007/978-3-642-45881-1_1)  
642 10.1007/978-3-642-45881-1\_1.

643 Gelaro, R., and Coauthors, 2017: The Modern-Era Retrospective Analysis for Research and  
644 Applications, Version 2 (MERRA-2). *Journal of Climate*, **30** (14), 5419–5454, [https://doi.org/](https://doi.org/10.1175/JCLI-D-16-0758.1)  
645 10.1175/JCLI-D-16-0758.1.

646 Genio, A. D. D., R. K. Achterberg, K. H. Baines, F. M. Flasar, P. L. Read, A. Sánchez-Lavega,  
647 and A. P. Showman, 2009: Saturn atmospheric structure and dynamics. *Saturn from Cassini-*  
648 *Huygens*, M. K. Dougherty, L. W. Esposito, and S. M. Krimigis, Eds., Springer Netherlands,  
649 113–159.

650 Gierasch, P. J., 1975: Meridional circulation and the maintenance of the Venus atmospheric  
651 rotation. *Journal of the Atmospheric Sciences*, **32** (6), 1038–1044, [https://doi.org/10.1175/](https://doi.org/10.1175/1520-0469(1975)032<1038:MCATMO>2.0.CO;2)  
652 1520-0469(1975)032<1038:MCATMO>2.0.CO;2.

653 Gill, A. E., 1980: Some simple solutions for heat-induced tropical circulation. *Quarterly Journal*  
654 *of the Royal Meteorological Society*, **106** (449), 447–462.

655 GMAO (Global Modeling and Assimilation Office), 2015: MERRA-2 inst3\_3d\_asm\_Np: 3d,  
656 3-Hourly, Instantaneous, Pressure-Level, Assimilation, Assimilated Meteorological Fields  
657 V5.12.4, Greenbelt, MD, USA, Goddard Earth Sciences Data and Information Services Center  
658 (GES DISC), Accessed: Sept 2021, 10.5067/QBZ6MG944HW0.

659 Grise, K. M., and D. W. J. Thompson, 2012: Equatorial planetary waves and their signature in  
660 atmospheric variability. *Journal of the Atmospheric Sciences*, **69** (3), 857–874.

661 Held, I. M., and A. Y. Hou, 1980: Nonlinear axially symmetric circulations in a nearly inviscid  
662 atmosphere. *Journal of the Atmospheric Sciences*, **37** (3), 515–533, [https://doi.org/10.1175/](https://doi.org/10.1175/1520-0469(1980)037<0515:NASCIA>2.0.CO;2)  
663 1520-0469(1980)037<0515:NASCIA>2.0.CO;2.

664 Herbert, C., R. Caballero, and F. Bouchet, 2020: Atmospheric bistability and abrupt transitions  
665 to superrotation: Wave–jet resonance and Hadley cell feedbacks. *Journal of the Atmospheric*  
666 *Sciences*, **77** (1), 31–49.

- Hersbach, H., and Coauthors, 2020: The era5 global reanalysis. *Quarterly Journal of the Royal Meteorological Society*, **146** (730), 1999–2049, <https://doi.org/10.1002/qj.3803>.
- Hide, R., 1969: Dynamics of the atmospheres of the major planets with an appendix on the viscous boundary layer at the rigid bounding surface of an electrically-conducting rotating fluid in the presence of a magnetic field. *Journal of the Atmospheric Sciences*, **26** (5), 841–853.
- Hide, R., 1970: Equatorial jets in planetary atmospheres. *Nature*, **225** (5229), 254–255, <https://doi.org/10.1038/225254b0>.
- Hide, R., and P. Mason, 1975: Sloping convection in a rotating fluid. *Advances in Physics*, **24** (1), 47–100, <https://doi.org/10.1080/00018737500101371>.
- Hill, S. A., S. Bordoni, and J. L. Mitchell, 2019: Axisymmetric constraints on cross-equatorial Hadley cell extent. *Journal of the Atmospheric Sciences*, **76** (6), 1547–1564.
- Horinouchi, T., and Coauthors, 2020: How waves and turbulence maintain the super-rotation of Venus’ atmosphere. *Science*, **368** (6489), 405–409.
- Hoskins, B., R. Neale, M. Rodwell, and G.-Y. Yang, 1999: Aspects of the large-scale tropical atmospheric circulation. *Tellus A: Dynamic Meteorology and Oceanography*, **51** (1), 33–44.
- Kalnay, E., and Coauthors, 1996: The ncep/ncar 40-year reanalysis project. *Bulletin of the American Meteorological Society*, **77** (3), 437 – 472, [https://doi.org/10.1175/1520-0477\(1996\)077<0437: TNYRP>2.0.CO;2](https://doi.org/10.1175/1520-0477(1996)077<0437: TNYRP>2.0.CO;2).
- KOBAYASHI, S., and Coauthors, 2015: The jra-55 reanalysis: General specifications and basic characteristics. *Journal of the Meteorological Society of Japan. Ser. II*, **93** (1), 5–48, <https://doi.org/10.2151/jmsj.2015-001>.
- Kostiuk, T., and Coauthors, 2006: Stratospheric global winds on Titan at the time of Huygens descent. *Journal of Geophysical Research: Planets*, **111** (E7).
- Kraucunas, I., and D. L. Hartmann, 2005: Equatorial superrotation and the factors controlling the zonal-mean zonal winds in the tropical upper troposphere. *Journal of the Atmospheric Sciences*, **62** (2), 371–389.

693 Laraia, A. L., and T. Schneider, 2015: Superrotation in terrestrial atmospheres. *Journal of the*  
694 *Atmospheric Sciences*, **72** (11), 4281–4296.

695 Lee, S., 1999: Why are the climatological zonal winds easterly in the equatorial upper troposphere?  
696 *Journal of the Atmospheric Sciences*, **56** (10), 1353–1363.

697 Lewis, N. T., G. J. Colyer, and P. L. Read, 2021: Characterizing regimes of atmospheric circulation  
698 in terms of their global superrotation. *Journal of the Atmospheric Sciences*, **78** (4), 1245–1258.

699 Lindzen, R. S., and A. V. Hou, 1988: Hadley circulations for zonally averaged heating centered off  
700 the equator. *Journal of the Atmospheric Sciences*, **45** (17), 2416–2427.

701 Liou, Y.-A., and S. Ravindra Babu, 2020: ENSO signatures observed in tropical tropopause layer  
702 parameters using long-term COSMIC RO data. *GPS Solutions*, **24** (4), 98.

703 Lutsko, N. J., 2017: The response of an idealized atmosphere to localized tropical heating:  
704 superrotation and the breakdown of linear theory. *Journal of the Atmospheric Sciences*, **75** (1),  
705 3–20.

706 Manney, G. L., M. I. Hegglin, and Z. D. Lawrence, 2021: Seasonal and regional signatures  
707 of ENSO in upper tropospheric jet characteristics from reanalyses. *Journal of Climate*, (22),  
708 9181–9200.

709 Matsuno, T., 1966: Quasi-geostrophic motions in the equatorial area. *Journal of the Meteorological*  
710 *Society of Japan. Ser. II*, **44** (1), 25–43.

711 Mitchell, J. L., and G. K. Vallis, 2010: The transition to superrotation in terrestrial atmospheres.  
712 *Journal of Geophysical Research: Planets*, **115** (E12).

713 Mitchell, J. L., G. K. Vallis, and S. F. Potter, 2014: Effects of the seasonal cycle on superrotation  
714 in planetary atmospheres. *The Astrophysical Journal*, **787** (1), 23.

715 NOAA (National Oceanic and Atmospheric Administration), 2020: Climate Prediction Cen-  
716 ter - four El Niño regions. URL [https://www.cpc.ncep.noaa.gov/products/analysis\\_monitoring/](https://www.cpc.ncep.noaa.gov/products/analysis_monitoring/ensostuff/nino_regions.shtml)  
717 [ensostuff/nino\\_regions.shtml](https://www.cpc.ncep.noaa.gov/products/analysis_monitoring/ensostuff/nino_regions.shtml), accessed Sept 2020.

718 NOAA (National Oceanic and Atmospheric Administration), 2021: Cold and warm episodes by  
 719 season. URL [https://origin.cpc.ncep.noaa.gov/products/analysis\\_monitoring/ensostuff/ONI\\_v5.](https://origin.cpc.ncep.noaa.gov/products/analysis_monitoring/ensostuff/ONI_v5.php)  
 720 [php](https://origin.cpc.ncep.noaa.gov/products/analysis_monitoring/ensostuff/ONI_v5.php), accessed Sept 2021.

721 Norton, W. A., 2006: Tropical wave driving of the annual cycle in tropical tropopause temperatures.  
 722 Part II: Model results. *Journal of the Atmospheric Sciences*, **63** (5), 1420–1431.

723 Peralta, J., R. Hueso, and A. Sánchez-Lavega, 2007: A reanalysis of Venus winds at two cloud  
 724 levels from Galileo SSI images. *Icarus*, **190** (2), 469–477, [https://doi.org/10.1016/j.icarus.2007.](https://doi.org/10.1016/j.icarus.2007.03.028)  
 725 03.028.

726 Pierrehumbert, R. T., and M. Hammond, 2019: Atmospheric circulation of tide-locked exoplanets.  
 727 *Annual Review of Fluid Mechanics*, **51** (1), 275–303.

728 Pinto, J. R. D., and J. L. Mitchell, 2016: Wave–mean flow interactions and the maintenance of  
 729 superrotation in a terrestrial atmosphere. *Journal of the Atmospheric Sciences*, **73** (8), 3181–  
 730 3196.

731 Polichtchouk, I., and J. Y.-K. Cho, 2016: Equatorial superrotation in Held and Suarez like flows  
 732 with weak equator-to-pole surface temperature gradient. *Quarterly Journal of the Royal Meteorological Society*, **142** (696), 1528–1540.

734 Potter, S. F., G. K. Vallis, and J. L. Mitchell, 2013: Spontaneous superrotation and the role of  
 735 Kelvin waves in an idealized dry GCM. *Journal of the Atmospheric Sciences*, **71** (2), 596–614.

736 Sakai, S., 1989: Rossby-Kelvin instability: a new type of ageostrophic instability caused by a  
 737 resonance between Rossby waves and gravity waves. *Journal of Fluid Mechanics*, **202**, 149–176.

738 Saravanan, R., 1993: Equatorial superrotation and maintenance of the general circulation in  
 739 two-level models. *Journal of the Atmospheric Sciences*, **50** (9), 1211–1227, [https://doi.org/](https://doi.org/10.1175/1520-0469(1993)050<1211:ESAMOT>2.0.CO;2)  
 740 10.1175/1520-0469(1993)050<1211:ESAMOT>2.0.CO;2.

741 Schneider, T., 2006: The general circulation of the atmosphere. *Annual Review of Earth and*  
 742 *Planetary Sciences*, **34** (1), 655–688.

- 743 Schneider, T., and S. Bordoni, 2008: Eddy-mediated regime transitions in the seasonal cycle  
744 of a Hadley circulation and implications for monsoon dynamics. *Journal of the Atmospheric*  
745 *Sciences*, **65** (3), 915–934, <https://doi.org/10.1175/2007JAS2415.1>.
- 746 Seiff, A., 2000: Dynamics of Jupiter’s atmosphere. *Nature*, **403** (6770), 603–605, [https://doi.org/](https://doi.org/10.1038/35001171)  
747 [10.1038/35001171](https://doi.org/10.1038/35001171).
- 748 Showman, A. P., and L. M. Polvani, 2010: The Matsuno-Gill model and equatorial superrotation.  
749 *Geophysical Research Letters*, **37** (18), <https://doi.org/10.1029/2010GL044343>.
- 750 Showman, A. P., and L. M. Polvani, 2011: Equatorial superrotation on tidally locked exoplanets.  
751 *The Astrophysical Journal*, **738** (1), 71, <https://doi.org/10.1088/0004-637X/738/1/71>.
- 752 Sobel, A. H., and T. Schneider, 2009: Single-layer axisymmetric model for a Hadley circulation  
753 with parameterized eddy momentum forcing. *Journal of Advances in Modeling Earth Systems*,  
754 **1** (3), <https://doi.org/10.3894/JAMES.2009.1.10>.
- 755 Sobel, A. H., and T. Schneider, 2013: Correction to “Single-layer axisymmetric model for a Hadley  
756 circulation with parameterized eddy momentum forcing”. *Journal of Advances in Modeling*  
757 *Earth Systems*, **5** (3), 654–657.
- 758 Suarez, M. J., and D. G. Duffy, 1992: Terrestrial superrotation: A bifurcation of the general  
759 circulation. *Journal of the Atmospheric Sciences*, **49** (16), 1541–1554.
- 760 Thompson, R. O. R. Y., 1971: Why there is an intense eastward current in the north atlantic but  
761 not in the south atlantic. *Journal of Physical Oceanography*, **1** (3), 235 – 237.
- 762 Tsai, S.-M., I. Dobbs-Dixon, and P.-G. Gu, 2014: Three-dimensional structures of equatorial  
763 waves and the resulting super-rotation in the atmosphere of a tidally locked hot Jupiter. *The*  
764 *Astrophysical Journal*, **793** (2), 141.
- 765 Tziperman, E., and B. Farrell, 2009: Pliocene equatorial temperature: Lessons from atmospheric  
766 superrotation. *Paleoceanography*, **24** (1).
- 767 Wang, P., and J. L. Mitchell, 2014: Planetary ageostrophic instability leads to superrotation.  
768 *Geophysical Research Letters*, **41** (12), 4118–4126.

- 769 Williams, G. P., 2003: Barotropic instability and equatorial superrotation. *Journal of the Atmo-*  
770 *spheric Sciences*, **60** (17), 2136 – 2152.
- 771 Yamazaki, K., T. Nakamura, J. Ukita, and K. Hoshi, 2020: A tropospheric pathway of the strato-  
772 spheric Quasi-Biennial Oscillation (QBO) impact on the boreal winter polar vortex. *Atmospheric*  
773 *Chemistry and Physics*, **20** (8), 5111–5127.
- 774 Yang, G.-Y., B. Hoskins, and L. Gray, 2012: The influence of the QBO on the propagation of  
775 equatorial waves into the stratosphere. *Journal of the Atmospheric Sciences*, **69** (10), 2959 –  
776 2982, <https://doi.org/10.1175/JAS-D-11-0342.1>.
- 777 Yang, W., R. Seager, and M. A. Cane, 2013: Zonal momentum balance in the tropical atmospheric  
778 circulation during the global monsoon mature months. *Journal of the Atmospheric Sciences*,  
779 **70** (2), 583–599.
- 780 Zurita-Gotor, P., 2019: The role of the divergent circulation for large-scale eddy momentum  
781 transport in the tropics. Part I: Observations. *Journal of the Atmospheric Sciences*, **76** (4),  
782 1125–1144.
- 783 Zurita-Gotor, P., A. Anaya-Benlliure, and I. M. Held, 2022: The sensitivity of superrotation to  
784 the latitude of baroclinic forcing in a terrestrial dry dynamical core. *Journal of the Atmospheric*  
785 *Sciences*, <https://doi.org/10.1175/JAS-D-21-0269.1>.
- 786 Zurita-Gotor, P., and I. M. Held, 2018: The finite-amplitude evolution of mixed Kelvin–Rossby  
787 wave instability and equatorial superrotation in a shallow-water model and an idealized gcm.  
788 *Journal of the Atmospheric Sciences*, **75** (7), 2299 – 2316.